

¹ PREPARED FOR SUBMISSION TO JINST

² **Directional Xenon Measurement**

³ ABSTRACT: Abstract...

⁴ KEYWORDS: Only keywords from JINST's keywords list please

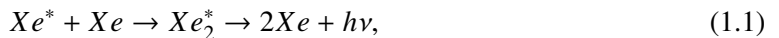
⁵ ARXIV EPRINT: [1234.56789](https://arxiv.org/abs/1234.56789)

6	Contents		
7	1	Introduction	1
8	2	Experimental Setup	2
9	2.1	The gas handling system	2
10	2.2	The cryogenic system	4
11	2.3	The detector system	5
12	2.4	The data acquisition system	7
13	3	Optical properties of the sphere	9
14	4	Detector sensitivity	9
15	5	Summary	12

16 1 Introduction

17 The use of Noble-liquid detectors in the field of astroparticle physics has increased in the past
18 decades. Detectors aiming at measuring Dark Matter (DM) particles and neutrinos properties use
19 large liquid argon or liquid xenon (LXe) chambers [1, 2]. Current and future experiment for DM
20 detection are tuned to detect weakly interacting massive particles (WIMPs), a postulated candidate
21 for DM particle [3]. LXe based detectors are to date the leading in sensitivity and size for these
22 searches [4–7].

23 When a particle interacts within the LXe media, it forms a cloud of excited and ionized states
24 with typical length of 100 nm. The excited Xe (Xe^*) combines with other Xe atoms to form an
25 excited dimer state (excimer) when they decay to ground state they emit light.



26 The electrons emitted from the ionization can recombine with a surrounding atom, this process of
27 recombination provides another possibility to produce excimers,



28 Once Xe^* is produced it adds to the scintillation process explained in 1.1. There are two types of Xe_2^*
29 excimer states, singlet and triplet, with lifetime of ~ 3 ns and ~ 25 ns respectively. The wavelength
30 emitted by these states is between (175-180) nm which is lower than the lowest excitation of xenon,
31 and therefore travel through it to reach a photo-detector situated outside the LXe. Although much is

32 measured on these scintillation processes, the basic knowledge of the quantum properties of these
33 interactions is based on experiments preformed several decades ago.

34 The phenomenon of superradiance in which identical quantum states "communicate" through
35 electromagnetic field if in close proximity, is well studied. In certain conditions the emission of
36 photons from these correlated states is very different then the sum of random states. This difference
37 is in spectral, temporal and spatial properties [8, 9]. Early studies show that scintillation in LXe can
38 produce coherent amplification of light [10, 11]. These studies were focusing on the macroscopic
39 ionization using high energy density electron beams.

40 The understanding and quantification of the microscopic effects of non linear phenomena such
41 as supperradiance in Lxe for a single interaction, can improve DM experiments to reduce background
42 by the extra knowledge of directionality. irreducible background such as coherent neutrino nucleus
43 scattering of neutrinos from the sun can be discard.

44 In this paper we present an experimental set-up called DIREXENO (DIREctional XENOn)
45 aiming at measuring the spatial distribution of LXe scintillation light, and quantify non-isotropic
46 emission.

47 2 Experimental Setup

48 In order to identify superradiance effects in LXe, the temporal and spatial properties of scintillation
49 events should be studied and quantified. In the DireXeno system LXe is circulated through a
50 small spherical cavity held in a thick sphere made of high purified fused silica (HPFS). The sphere
51 is surrounded ($\sim 4\pi$) by PMTs allowing high resolution spatial and temporal measurements of
52 individual photons. The PMTs do not come in contact with the xenon, so less impurities are
53 introduced to it, and the material selection is less stringent. The geometrical design of the system
54 approximates a point source of scintillation photons, and a detailed vertex reconstruction within the
55 LXe bubble is unnecessary. A schematic view of the system is shown in Fig 1 .

56 The current system is designed with ~ 1 ns time resolution, less than 1 ns synchronization
57 between PMTs, and ~ 8 radians spatial resolution. Since the exact nature and magnitude of
58 superradiance in LXe is yet unknown a guiding principle in the design was flexibility to upgrades
59 or redesign of any part of the system to fulfill any future experiment requirements. The modular
60 design allows gain fast and easy recovery in case of components malfunction.

61 The system is made of four main building blocks. (i) **The gas handling system** which in
62 normal working mode circulates the xenon and purifies it. (ii) **The cryogenic system**, liquefies the
63 xenon and delivers it to the detector system. (iii) **The detector system** consists of a fused silica
64 sphere that holds a small bubble of LXe target, and PMTs around the sphere. (iv) **The DAQ system**
65 supplies high voltage (HV) to the PMTs and handles monitoring, triggering and digitization of data.
66 The entire assembly is held on 3 separate racks as shown in Fig. 2.

67 2.1 The gas handling system

68 In DIREXENO only the prompt scintillation is measured, so a high level of LXe purity is not of a
69 great importance. However in many LXE detectors the desired level of impurity concentration is
70 at the level of 1 ppb O_2 equivalent [1] This is crucial to allow ionization electrons drift for several
71 cm. To reach that purity level in a reasonable amount

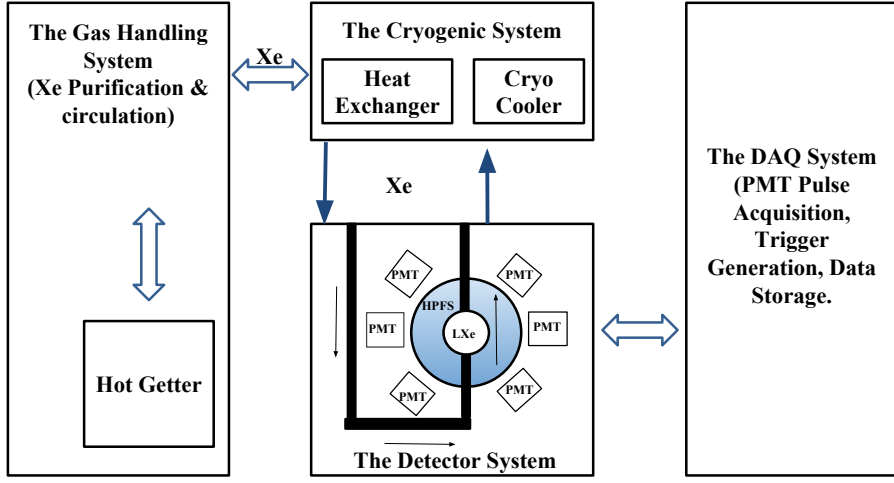


Figure 1. A schematic view of DIREXENO.

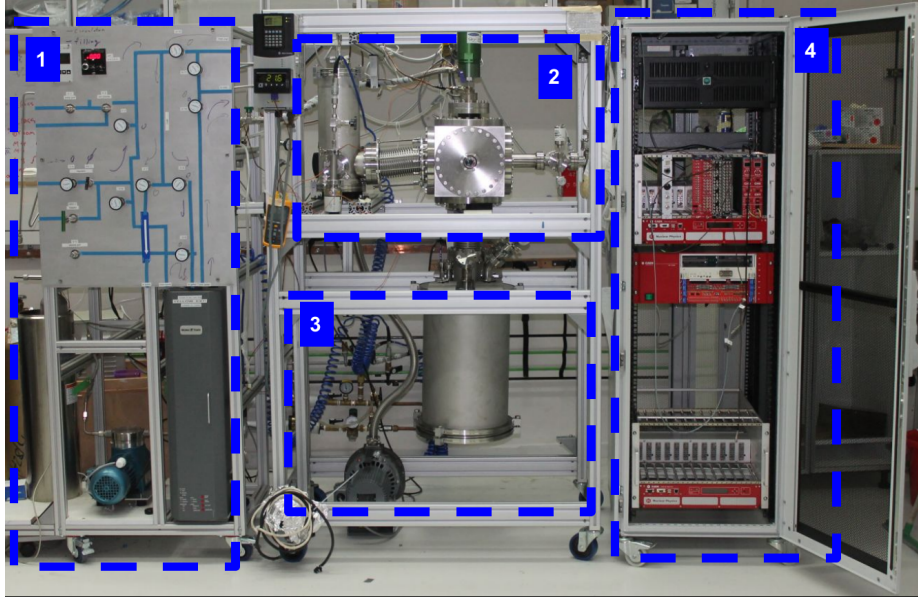


Figure 2. The DireXeno system mounted on the three racks. 1. The gas handling system. 2. The cryogenic system including the heat exchanger. 3. The detector chamber. 4. The Data acquisition system.

72 of time (several days instead of months), a continuous purification is needed. The gas handling
 73 system provides this process along with all gas handling operations such as filling and recuperation
 74 and circulation. The xenon circulation also plays a major role in heat transfer.

During purification, The xenon is forced by a circulation pump¹ extracting LXe from the detector part through a heat exchanger² where it is heated and vaporized, into a hot getter³ which cleans the xenon. The xenon passes through a mass flow controller⁴ (MFC), enabling monitoring and controlling the amount of heat introduced to the system. Once purified, the xenon is delivered back to the cryogenic system via the heat exchanger, where the remaining GXe is liquefied before flowing back to the detector part. A schematic of this system is shown in fig. 3.

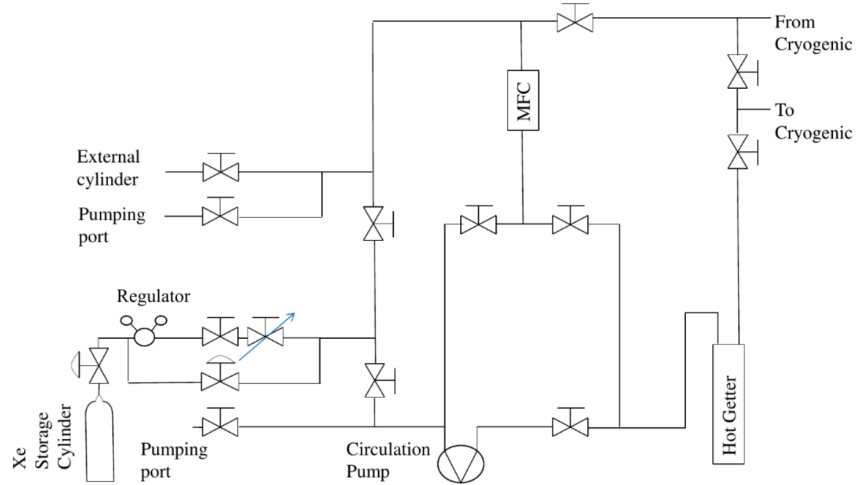


Figure 3. Schematics of the gas handling system. High pressure valves are indicated as valves with arcs. Needle valves are indicated as a valve with an arrow.

2.2 The cryogenic system

Remote cooling is generally used in LXe experiments due to reduction in background radiation and acoustic noise from the cooler to the detector, and due to design flexibility. The cryogenic system is connected to the gas handling system on one side and to the detector part on the other, and built such that replacing the cryo-cooler type (e.g., to PTR) requires just an adaptation to the top flange.

The cryogenic system is divided to an outer vessel (OV) which holds the insulation vacuum, and an inner vessel (IV) which holds the xenon. In addition to the vacuum which prevents heat leakage due to diffusion and convection, the IV is completely covered by multi layer aluminized Myler to prevent heating via radiation.

The OV is made of a 10" Conflat (CF) cube, with ports on all six faces, interfacing the gas handling system and the detector part, and bearing service ports (e.g., feed-throughs, pumping ports, view ports). The OV is connected to the detector part via a 6" CF flexible bellows, providing a shared vacuum.

The IV is made of 1.5" long cylinder with 6" CF flanges on both sides, holding xenon within. A 120 mm diameter cold finger is welded to its top flange. The design of the cold finger is similar to the one in [12]. The inner part of the cold finger is made of long fins, resulting in a better heat

¹N143 SN.12E AC 230V50HZ KNF diaphragm circulation pump

²GEA GBS100M-24 plate heat exchanger

³MONO-TORR PS4-MT15-R-2

⁴MKS mass flow controller 1179A00614CR1BM

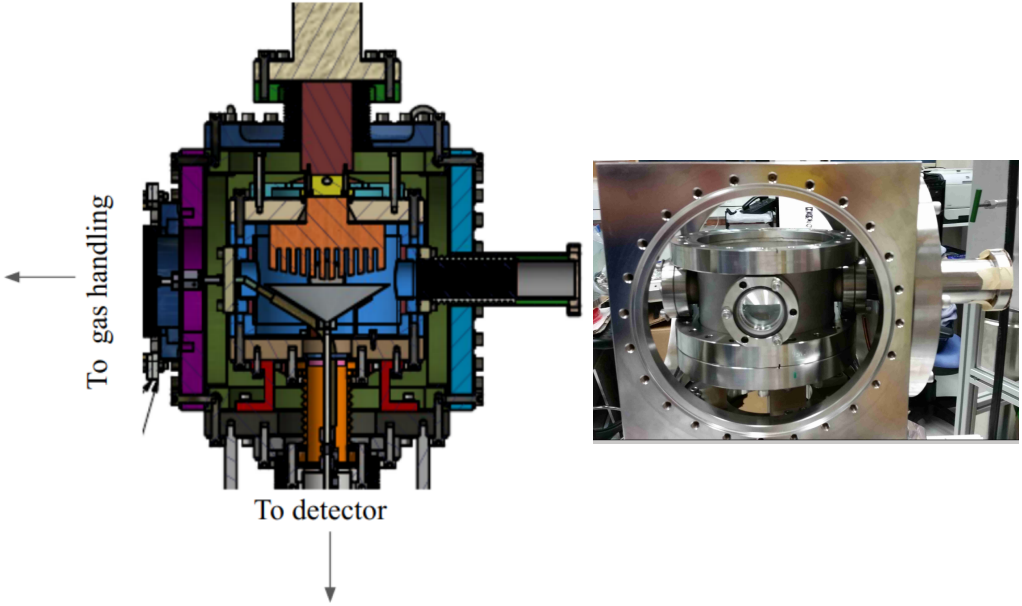


Figure 4. CAD view of the cryogenic system(Left) and a picture of the cryogenic system (Right) . The cryogenic system. (Left) CAD design view, (right) picture of the actual system.

97 transport. The upper part of the cold finger is in thermal contact with the QDrive cryo-cooler¹ via
 98 a copper adapter. The copper adapter holds two 100Ω pt resistor which are connected to a PID
 99 reader² for temperature measurements. A cartridge-heater is also inserted to the copper adapter for
 100 emergency heating in case xenon freezes on the cold finger.

101 The cryo-cooler is connected via a $4\frac{1}{2}$ " flange to the OV top flange. While usually cryo-coolers
 102 used for xenon experiments constantly operate in maximal cooling, the QDrive cryo-cooler utilizes
 103 a temperature control to vary its cooling power up to 70 W. This allows setting a desired working
 104 temperature which is constant within less than $0.1\text{ }^{\circ}\text{C}$ measured on the cryo-cooler.

105 On the inner side of the IV bottom flange a thin 0.6 mm SS funnel is installed collecting LXe
 106 drops from the cold finger, and delivering them to the detector. This flange is attached to the detector
 107 part, via a $3\frac{3}{8}$ " flexible bellows. The bellows hosts two pipes connected to the circulation system,
 108 and a third pipe coming from the funnel. The three pipes deliver LXe whereas the GXe is filling
 109 the bellows volume. The purer LXe (from the gas handling system) and the less pure LXe (from
 110 the cold finger) are separated, and can be delivered to different parts of the system. Some of the
 111 guidelines for the design of the cryogenic system are based on [13]. The CAD view of the design
 112 of the cryogenic system and a photo of the actual system are shown in Fig 4.

113 2.3 The detector system

114 The detector system refers to a vacuum chamber and its inner assembly consisting of a transparent
 115 sphere that contains the LXe, the PMT sensors observing it and their accessories. This chamber is
 116 placed below the cryogenic system.

¹QDrive 20BB 9p6 A 3 AYNBNCO

²cryo-con model 18i Cryogenic Temp Monitor

117 The interface unit to the cryogenic system is built out of two flanges welded together via seven
 118 tubes, which serve as service ports for electrical and other feedthroughs: four with a $2\frac{3}{4}$ " CF flange,
 119 and three with a $1\frac{1}{3}$ " CF flange (mini-CF). The upper flange, ISO-K NW320, shares the cryogenic
 120 system's OV insulation vacuum, while the bottom one, CF-10", is part of the IV and could hold
 121 xenon for future detectors. The CF flange is also adapted to fit a smaller CF-4 $\frac{5}{8}$ " flange which is
 122 currently used.

123 The vacuum chamber is made of an ISO-K NW320 nipple closed with a blank flange from
 124 below, the length of the nipple is determined such that the maximal height of the whole apparatus
 125 is 190 cm, allowing an easy transport of the detector through standard doors.

126 The 4 $\frac{5}{8}$ " CF flange is connected to a split vessel that serves as a LXe reservoir. one part is
 127 connected to the top of the HPFS sphere, and one to the bottom. LXe is circulated such that LXe
 128 coming from the gas system drips into one part and pumped from the other. This controls the liquid
 129 level, and the sphere is constantly filled with LXe.

130 The sphere is a custom designed hollow shell made of Corning HPFS 8655 with high trans-
 131mittance to VUV. Two Invar tubes with SS mini-CF flange are connected to the sphere on both
 132 sides. The technical design and photo of the sphere are shown in Fig. 5. The optical properties
 133 of the sphere will be further discussed in Sec. 3. The bottom flange of the sphere is held using a
 134 brass holder to prevent force or torque applied on the sphere while mounting it. The brass holder is
 135 connected to a plate held from the top CF-10" flange.

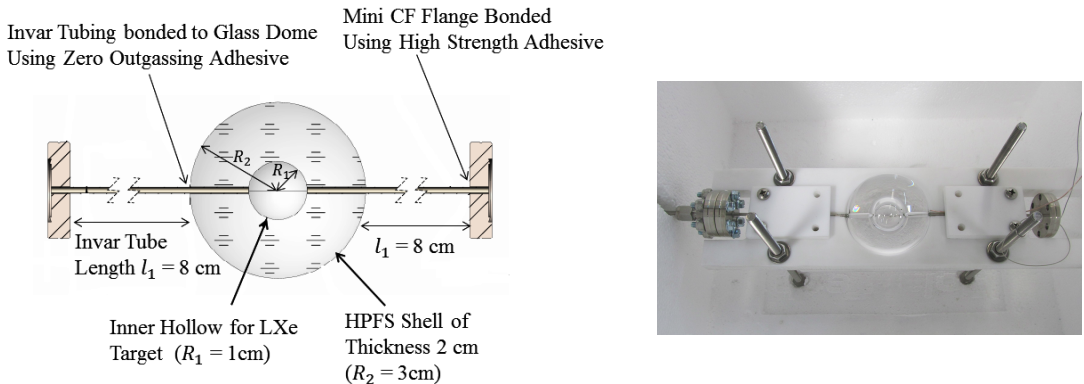


Figure 5. (Left)The technical design of the HPFS shell with Invar tubing and mini CF flanges. (Right) The industrially manufactured HPFS shell, held in a test fixture.

136 Photons emitted from the LXe in the sphere are detected by 20 PMTs¹. The PMTs are chosen
 137 to have a quantum efficiency greater than 30% at 178 nm. The gain of the PMTs is 2×10^6 at
 138 an applied voltage of 900 V . A positive voltage divider², is used to provide high voltage to the
 139 PMTs. The PMTs are held with a special aluminum holder, coated with anti-reflection substance.
 140 The holder is made of two hemispheres hosting the PMTs in 3 rows all of them pointing to the
 141 center of the sphere. The PMTs are attached to the holder by their voltage–divider bases using M2
 142 PEEK screws (see Fig 6). The CAD design and a photo of the detector system are shown in Fig. 7.

¹R8520-406 Hamamatsu 1" PMT, active area 20.5 mm \times 20.5mm

²Hamamatsu VDS18130p 24 channel positve polarity.

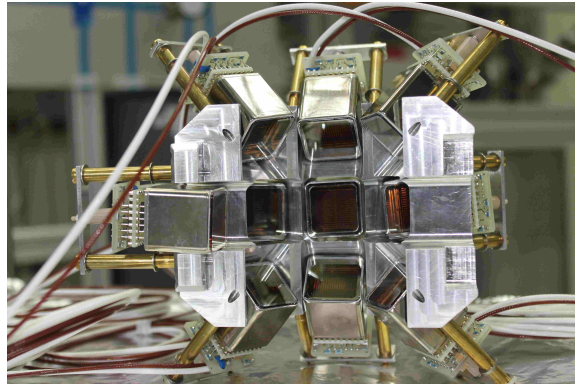


Figure 6. A PMT holder-hemisphere. Two identical hemispheres are used to hold the PMTS around the sphere.

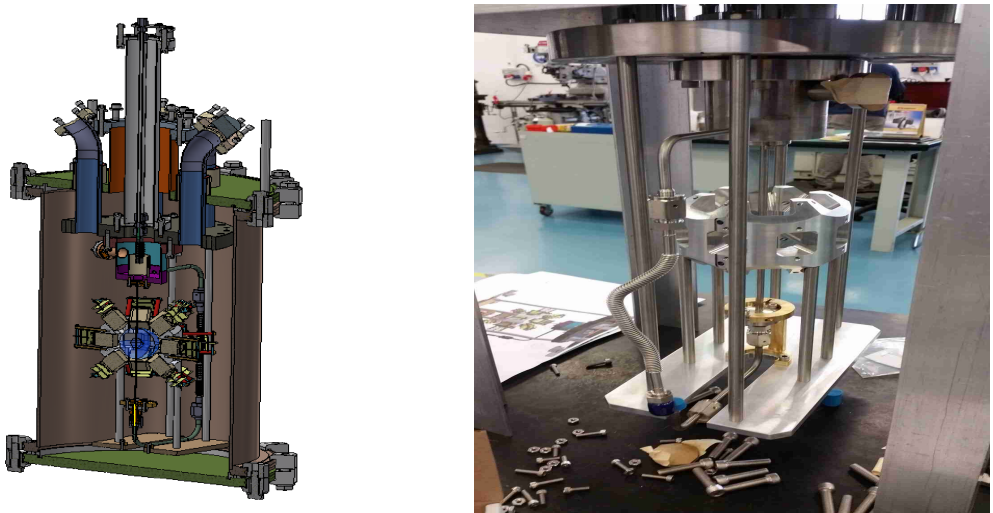


Figure 7. (Left) CAD design of the detector part. (Right) First mounting of the detector part, still not connected to the rest of the system.

2.4 The data acquisition system

The DAQ system is heterogeneous using both NIM and VME electronic modules. The data readout is being carried out through a PCIe card¹ connected via an optical link to a VME controller². A schematic layout of the DAQ system is shown in Fig. 8.

The PMTs are ramped up to +800V (the maximum is +900V) using VME high voltage distributor module³. The raw pulses from the PMTs are amplified and shaped using two PMT preamplifiers⁴. The preamplifier operates from DC to 275 MHz and produces two identical $50\ \Omega$ non inverting outputs with voltage gains of 10 for each PMT channel. One of the outputs is converted

¹CAEN A3818 PCIe

²CAEN V2718 VME controller

³iseg VDS18130p : 24 independent channels positive polarity voltage distributer

⁴Phillips 776. 16 independent and direct-coupled amplifiers channels

151 into a digital signal by an ADC¹, and the other to binary signals using two discriminators².

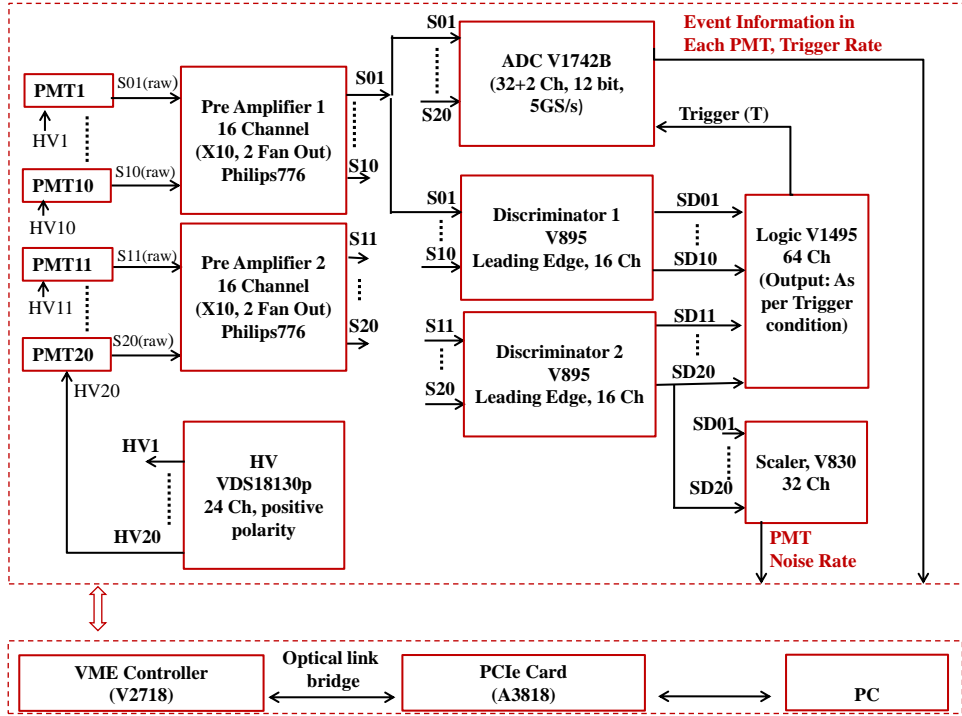


Figure 8. The schematic of the data acquisition system of DireXeno. The signal coming from 20 PMTs ($i = 1 - 20$) and the subsequent electronic channels to record the events once triggered. Where $S_i(\text{raw})$ is the raw electrical pulse output of the PMTs, S_i are the amplified pulses, and SD_i are the binary outputs from the discriminator. Why is VME controller in lower box? The controller has access to all the VME electronic modules. So it is difficult to put it in the upper box. Collectively, the controller has access to the upper box..

152 The ADC consists of two 12bit 5GS/s switched capacitor digitizer sections, each of them with
 153 16+1 channels, based on DRS4 chip. The dynamic range of the input signal is 1 Vpp with an
 154 adjustable DC offset. This module constantly samples (5GS/s, 2.5 GS/s or 2 GS/s) either bipolar
 155 or unipolar analog input signals, and records them into circular analog memory buffers. Once
 156 triggered, all analog memory buffers are frozen and digitized into a digital memory buffer with a
 157 12 bit resolution. The binary output signals from the discriminator are duplicated and fed to the
 158 logic module³ and to a scaler⁴. A global majority trigger is generated in the logic module with
 159 the coincidence of any two out of the twenty PMTs within a time window of XXX ns. 100 ns is
 160 probably a reasonable limit.. The event information and trigger rate are read from the ADC, while
 161 the individual PMTs trigger rate from the scaler. Further analyses of the relevant events are carried
 162 out offline.

¹CAEN ADC V1742: switched capacitor digitizer

²CAEN V895 16 channel leading edge discriminator

³CAEN V1495: FPGA based general purpose VME board

⁴CAEN V830: 16 channel scalar

163 3 Optical properties of the sphere

164 The central component of the experiment is the HPFS sphere, which holds the LXe target, located
 165 in the center of the detector system. The sphere is made of two Corning HPFS 8655 hemispheres
 166 attached by a UV transparent glue. The refractive index of this HPFS is 1.58 at 185 nm, matching
 167 to the LXe one, which is 1.61. Hence, there is minimal diffraction from the original direction
 168 of the photons as they transit from the LXe target to the sphere. The refractive index at various
 169 wavelengths are shown in Fig. 9 (left panel).

170 The HPFS transparency to VUV photons is an extremely crucial parameter for setting the
 171 sphere's dimensions (inner and outer radii). Therefore, the transmittance of an HPFS sample was
 172 measured, using a VUV monochromator light source. The measured transmittances as a function
 173 of wavelength are shown in Fig. 9 (right panel). The transmittance of the sample at 178 nm,
 174 is $\sim 98.7\%/\text{cm}$.

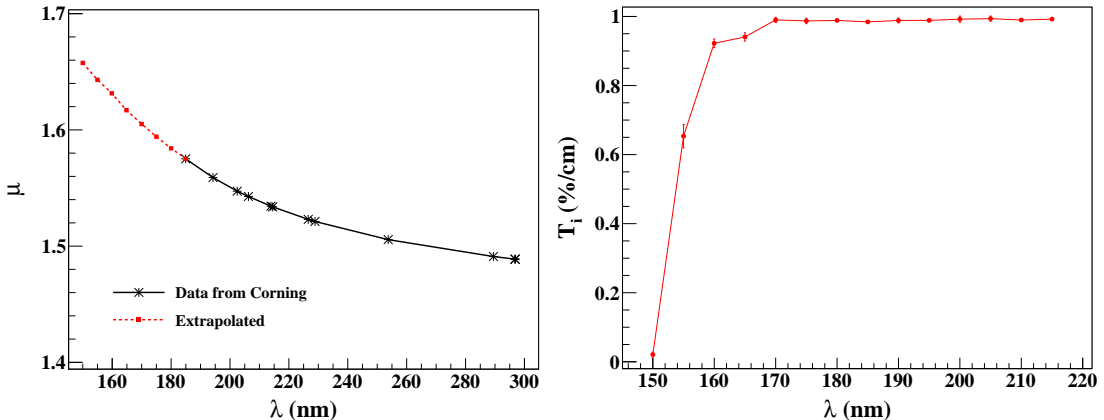


Figure 9. Some relevant characteristics of HPFS-8655. (Left) The refractive index as provided by corning and extrapolated to relevant wavelength range. (Right) The measured internal transmittance (T_i), the mean and RMS obtained from 10 sets of measurements are shown.

175 The sources that will be used for exciting the xenon, and creating the superradiance (signal)
 176 as well as the standard emission (background), will be ^{137}Cs ($E_\gamma=662\text{ keV}$) and ^{57}Co ($E_\gamma=122\text{keV}$
 177 & 136 keV) for ER with mean free path of $\sim 4\text{ cm}$ and $\sim 1\text{ cm}$ respectively. For NR $^{241}\text{AmBe}$, D-D
 178 neutron generator, or neutron produced in an accelerator will be used.

179 Using a GEANT4 based simulation [?] studying the path of the scintillation photons the
 180 sphere dimensions are optimized. The shell should be thick enough to reduce internal reflections,
 181 but not too thick to attenuate the scintillation light. The LXe target bubble within should not be too
 182 large in order to avoid double scatters. The outer radius is 3 cm, and the inner (the hollow space
 183 that holds the LXe) is 1 cm.

184 4 Detector sensitivity

185 The sensitivity of the detector is estimated by its ability to identify an anisotropic component in the
 186 scintillation photons emission pattern (signal), over the isotropic one (background). The photon

187 emission pattern is modeled using a combination of isotropic emission and one or two beams:

$$\mathcal{F}(\theta, \phi) = (1 - r_{aniso}) \cdot f_{iso} + r_{aniso} \cdot [r_1 f_G(\sigma_1) + r_2 f_G(\sigma_2)], \quad (4.1)$$

188 where f_{iso} is the PDF of an isotropic emission, f_G is a PDF of a Gaussian distribution with half
 189 width σ . r_{aniso} is the anisotropic emission fraction, and $r_{1,2}$ are the relative beams intensities. The
 190 first beam direction is random, and the second's is either random ("uncorrelated") or opposite to
 191 the first's ("correlated"). The different emission patterns used here are summarized in Table 1.

Table 1. Anisotropic emission patterns. For all patterns $r_{aniso} = 0.1$

Pattern no.	No. of beams	type	Beam half widths		Signal fractions		N'
			σ_1	σ_2	r_1	r_2	
1	1	single beam	5°	-	1	0	3200
2	1	single beam	15°	-	1	0	4630
3	2	correlated	5°	5°	0.5	0.5	4520
4	2	correlated	15°	15°	0.5	0.5	9770
5	2	uncorrelated	5°	5°	0.5	0.5	9370
6	2	uncorrelated	5°	10°	0.5	0.5	19500
7	2	uncorrelated	15°	15°	0.5	0.5	28200
8	2	uncorrelated	10°	30°	0.5	0.5	49900
9	2	uncorrelated	10°	30°	0.2	0.8	56000
10	2	uncorrelated	30°	10°	0.2	0.8	43000

192 A GEANT4 based simulation is used to model the detector system, generate photons, propagate
 193 them through the detector, and obtain a PMT hit pattern. The photons detected at the PMTs are
 194 mapped and put through a statistical test to check the detector's sensitivity towards the different
 195 emission patterns.

196 The relevant geometrical and optical parameters, which are used in the simulation, are listed
 197 in Table 2. The scintillation light produced in a particular event is emitted by a cloud of excimers.
 198 This cloud is assumed to have a linear size much smaller than that of the optical system. Therefore
 199 each event is simulated as a number of photons that are emitted from a point in the LXe with
 200 some emission pattern (see Table 1). The number of generated photons for each event is taken to
 201 be Poisson(50), which correspond to an energy deposition of $\sim 2.5\text{keV}$ or $\sim 7\text{keV}$ for ER or NR
 202 respectively. The LXe target is much smaller than the mean free path of the source particles, and to
 203 account for that the events are uniformly generated in the LXe volume. The probability for a photon
 204 being transmitted/reflected at a given surface is determined by Fresnel's equations, which include
 205 Snell's law for the transmitted light, and specular reflection for the reflected light. The boundary
 206 surfaces between different media such as, the LXe–HPFS, HPFS–vacuum and vacuum–PMT, are
 207 assumed to be perfectly smooth, therefore enabling only specular reflection. The photons reaching
 208 the PMTs can either be detected, absorbed or reflected from the photocathode or PMT window. A
 209 simplified approach of the above possibilities is considered: a photon reaching the PMT has a 30%
 210 probability to be detected (since the PMTs have $\text{QE} \geq 30\%$), 50% probability to get absorbed and
 211 20% probability to get specularly reflected.

Table 2. The parameters used in simulation

Parameter	Value	Parameter	Value
LXe absorption length	100 cm	HPFS shell inner radius	1cm
LXe scattering length	35 cm	HPFS shell thickness	2 cm
LXe refractive index	1.61	PMT QE	30%
LXe Scintillation wavelength	178	PMT distance from center	39 mm
HPFS absorption length	100 cm	Number of PMT	20
HPFS refractive index	1.57	PMT active area	22mm × 22mm
HPFS scattering length	∞	Invar tube diameter	1 mm

212 The statistical fluctuation in the electronic signal generated in a PMT for a certain number
 213 of incident photon is taken into account. The R8520 PMTs have 20% probability for double
 214 photoelectric emission for 178 nm photons, which is included in the simulation. Each detected
 215 photon on a PMT is assigned a uniformly random position on the PMT surface. The direction of
 216 this point with respect to the center of the LXe sphere is defined as the incident direction of the
 217 photon. The direction information is then used to calculate the angles between all possible pairs of
 218 photon for any event and calculate the correlation between all angle pairs. **Do you want to add fig
 219 of correlations iso and aniso? Good idea. Iso and a few choses aniso are fine?**

220 In order to quantify the anisotropicity of the emission, the angle correlation distribution of an
 221 anisotropic hit pattern is compared to that of the isotropic pattern. A χ^2 test statistics is used where
 222 the reduced χ^2 is defined as:

$$\chi^2_{\nu} = \frac{1}{\nu} \sum_{i=1}^{\nu} \frac{(O_i - E_i)^2}{E_i}, \quad (4.2)$$

223 where E_i is the expected number of entries for an isotropic emission obtained from a sample
 224 of 10^5 simulated events. O_i is the observed number of entries, and ν is the total number of angle
 225 correlation bins which is also the degree of freedom. Sixty bins of identical width are used.

226 To asses the needed exposure to claim discovery assuming one of the pattern mentioned above,
 227 10^4 data sets are generated and tested against the null hypothesis. This is repeated for increasing
 228 number of events between 1 – 4000 assuming different values of the anisotropy fraction (r_{aniso}).
 229 The $\langle \chi^2_{\nu} \rangle$ and its 2σ band for pattern 1, assuming $r_{aniso} = 0.1$ overlaid with the corresponding
 230 values for an isotropic emission are shown in Fig. 10. The values of N' , required to claim 5σ
 231 discovery, for different values of r_{aniso} are calculated for each pattern as illustrated in Fig. 11. The
 232 number of events N' for $r_{aniso} = 0.1$ are summarized in Table 1 for all emission patterns.

233 A simulation with two typical sources that emit isotropically, a $10 \mu\text{Ci}^{137}\text{Cs}$ (662 keV gamma),
 234 and a $2.7 \mu\text{Ci}$ AmBe (5 MeV neutron), shows that for an average yield of 50photons/event, the rate
 235 of events in the detector is: 1.25×10^4 events/day for NR and 625 events/day for ER. Therefore a
 236 system that can operate stably for few weeks is expected to do reasonable measurements for ER and
 237 NR events.

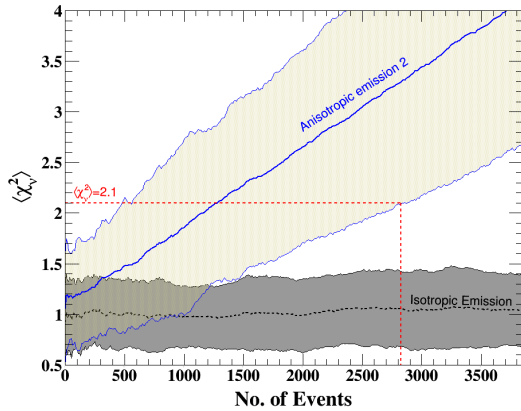


Figure 10. $\langle \chi^2 \rangle$ and its 2σ band for isotropic emission (black) and for pattern 2 (blue). The $\langle \chi^2 \rangle$ for isotropic emission fluctuate around 1 with $\sigma = 0.2$ which is consistent with the expected value of $\frac{1}{\sqrt{30}} \equiv 0.18$ for reduced χ^2 distribution with 60 degrees of freedom. ~ 3000 events are needed to claim 5σ discovery ($\chi^2 = 2.1$) for this emission pattern

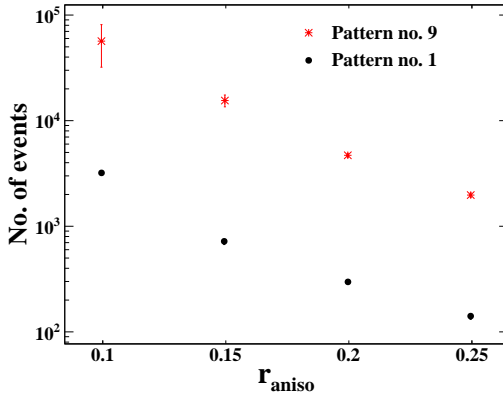


Figure 11. The number of events needed for each emission pattern to achieve 5σ presented only for pattern 1 and 9. Here $r_{aniso} = 0.1$. for four different values of r_{aniso} .

238 5 Summary

239 The setup of Direxeno, an experiment to measure the spatial and temporal distribution of LXe
 240 scintillation, has been presented. The system consists of 4 main building blocks (gas handling,
 241 cryogenic, detector, and DAQ), each of which can be exchanged without altering others allowing
 242 significant flexibility and modularity. Each of the building blocks has been described in detail, with
 243 emphasis on the design and components.

244 The sensitivity of the setup to different postulated non isotropic emission patterns are studied
 245 using MC simulations. For the patterns studied, a run-time of 2-3 weeks is required using typical
 246 radioactive sources. Therefore the system is designed to maintain stability over a reasonable time
 247 period.

248 Using DireXeno, effects like superradiance or any other non-linear scintillation can be mea-
 249 sured. Measuring the correlation between the direction of the emission and the direction of the

250 radioactive source, may lead to directionality measurement which will allow enhanced statistical
251 modeling of background and improved sensitivity in DM experiments.

252 References

- 253 [1] E. Aprile and T. Doke. Liquid Xenon Detectors for Particle Physics and Astrophysics. *Rev. Mod.*
254 *Phys.*, 82:2053–2097, 2010.
- 255 [2] A. Rubbia. Future liquid Argon detectors. 2013. [*Nucl. Phys. Proc. Suppl.* 235-236, 190(2013)].
- 256 [3] J. Silk et al. *Particle Dark Matter: Observations, Models and Searches*. Cambridge Univ. Press,
257 Cambridge, 2010.
- 258 [4] E. Aprile et al. First Dark Matter Search Results from the XENON1T Experiment. 2017.
- 259 [5] D. S. Akerib et al. Results from a search for dark matter in the complete LUX exposure. *Phys. Rev.*
260 *Lett.*, 118(2):021303, 2017.
- 261 [6] Changbo Fu et al. Spin-Dependent Weakly-Interacting-Massive-Particle–Nucleon Cross Section
262 Limits from First Data of PandaX-II Experiment. *Phys. Rev. Lett.*, 118(7):071301, 2017.
- 263 [7] J. Aalbers et al. DARWIN: towards the ultimate dark matter detector. *JCAP*, 1611:017, 2016.
- 264 [8] R. H. Dicke. Coherence in spontaneous radiation processes. *Phys. Rev.*, 93:99–110, Jan 1954.
- 265 [9] M. Gross and S. Haroche. Superradiance: An essay on the theory of collective spontaneous emission.
266 *Physics Reports*, 93(5):301 – 396, 1982.
- 267 [10] N G Basov, V A Danilychev, and Yurii M Popov. Stimulated emission in the vacuum ultraviolet
268 region. *Soviet Journal of Quantum Electronics*, 1(1):18, 1971.
- 269 [11] Frederick H. Mies. Stimulated emission and population inversion in diatomic bound-continuum
270 transitions. *Molecular Physics*, 26(5):1233–1246, 1973.
- 271 [12] E. Aprile et al. The XENON100 Dark Matter Experiment. *Astropart. Phys.*, 35:573–590, 2012.
- 272 [13] K L Giboni, X Ji, H Lin, A Tan, T Ye, Y Zhang, and L Zhao. A liquid xenon development and test
273 system. *Journal of Instrumentation*, 9(04):T04006, 2014.